Chapter 4

Angle-dependent reflectivity from elastic reverse-time migration

Any amplitude-based lithologic inversion method must compensate for all changes in the amplitudes that are not directly related to the properties to be estimated. Conventional methods for compensation of geometrical spreading and transmission/conversion losses are not applicable when the subsurface structures cannot be reasonably approximated by horizontal layers. Migration-based methods have been recently proposed to improve the estimation of angle-dependent reflectivity in the presence of complex structures. This chapter evaluates the use of different imaging conditions for anisotropic prestack reverse-time migration to estimate the reflectivity as a function of the local illumination angle. Emphasis is given to the plane-wave-response criterion which is used in the imaging stage of the plane-wave-response migration. This migration method generates four simultaneous images which correspond to the in-depth (local) plane-wave response for PP, PS, SP, and SS reflections, and can be used in a Zoeppritz-based elastic inversion scheme.

4.1 Introduction

Different methods for retrieving the angle-dependent reflection coefficient from surface seismic data have been described in the geophysical literature. In a classic paper, O'Doherty and Anstey (1971) analyzed the relative importance of a large number of factors in the final amplitude of recorded reflections. Any inversion method that attempts to retrieve rock properties from amplitude information must compensate for all the factors that are

not directly related to such properties. This study focuses on those factors that are affected by the long-wavelength elastic characteristics of the medium, that is, geometrical spreading and transmission/conversion losses.

Initial methods for recovering the angle-dependent reflectivity function were based on the assumption that the subsurface layers are nearly horizontal within the range covered by a common midpoint (CMP) gather, which is the basic assumption of standard CMP processing (Newman, 1973; Yu, 1985; Kolb and Chapel, 1989; Cunha, 1990). Although these methods properly compensate for the long wavelength losses in a reasonable number of practical problems, they cannot be applied to areas with structurally complex geology.

Recently, more powerful methods for estimating angle-dependent reflectivity, based on migration algorithms, have been developed. De Bruin et al. (1990a) presented a method for estimating angle-dependent reflectivity using a scalar prestack x-ω migration scheme. First, the multicomponent data were decomposed into PP, PS, SP, and SS modes and each of them migrated separately. Tests with synthetic data showed that the method was able to retrieve the reflectivity function with considerable accuracy for horizontal layers, but when dip was present (de Bruin et al., 1990b), the retrieved function was incorrectly shifted (in angle) because of the assumption of a horizontally-layered earth which is implicit in their imaging principle (integration along constant Snell parameter traces). Another limitation of their method is that the estimated reflectivities do not correspond to the local, in-depth reflectivities because the decomposition is carried out before the depth extrapolation. As a result, a wavefield that leaves and arrives at the surface as a pure compressional mode (marine data), but is associated with an SS reflection (PSSP mode) cannot be imaged by their method. Lumley and Beydoun (1991) introduced a different method for retrieving the reflectivity function, using an elastic, prestack Kirchhoff migration scheme. Their imaging principle was not limited by the horizontal layer assumption and was successfully applied to synthetic and real data. However, as a consequence of the Kirchhoff approach, their method suffers from the restrictions imposed by the ray approximation associated with the evaluation of the Green's function. Moreover, both methods assume that the medium is isotropic and attempt to image only the converted modes associated with a single conversion at the reflection plane. Therefore, when applied to offshore data, these approaches can obtain only PP reflectivities.

This chapter describes a method for retrieving angle-dependent reflectivity that is based on anisotropic, prestack reverse-time migration (RTM). Zero-offset reverse-time

migration was independently developed in the early 1980s by Whitmore (1983), Baysal et al. (1983), Kosloff and Baysal (1983), McMechan (1983), and Lowental and Mufty (1983). Levin (1984) gives a general description of the different formulations, clarifies the principle of reverse-time migration and shows how it relates to depth extrapolation methods. Etgen (1986), Faria et al. (1986), and Hellman et al. (1986), among others, extended the method to multi-offset prestack data. With two different approaches to the imaging condition, Mora (1986) and Chang and McMechan (1987) introduced an elastic isotropic formulation for RTM. Etgen (1987) extended the extrapolation step for the general anisotropic case, but was able to migrate only S_H modes because of the restriction imposed by the scalar formulation of the imaging condition. Karrenbach (1991) developed an anisotropic reverse-time migration/inversion scheme using a tensorial imaging condition represented by the crosscorrelation between the different components of the upcoming and downgoing wavefields. Each of the resulting images is associated with a perturbation in one component of the stiffness tensor. His approach is equivalent to the first step of a linearized inverse algorithm because it backward propagates the residuals between the forward-modeled and the recorded wavefields at the receivers, rather than just the recorded wavefield. As a result, the images were more closely related to perturbations in the impedance, instead of to the reflectivity functions.

Like the work developed by Karrenbach, the method described in this chapter uses an anisotropic, prestack, reverse-time migration algorithm. The time propagation uses the dual-operator modeling scheme described in chapter 3 instead of traditional finite-difference schemes. The formulation of the imaging condition condition leads to the generation of four images associated with the plane-wave, angle-dependent reflectivity functions for PP, PS, SP, and SS modes. This approach is closely related to the method described by de Bruin et al (1991), in which the surface data is downward extrapolated to the target level (redatuming) and tau-p transformed. In contrast to de Bruin's method, the plane-wave-response migration described in this chapter is neither restricted to the target zone, nor to the horizontal layer assumption for the target zone.

4.2 Different approaches to reverse-time migration

All migration methods involve the application of two steps: downward extrapolation in depth (or backward extrapolation in time) and an imaging principle. The specific form of

these two steps depends on the domain in which the migration is applied (e.g., space-time, spatial-wavenumber-frequency, tau-p), and whether it is applied before or after stack. This section focuses on the discussion of prestack reverse-time migration in the space-time domain.

4.2.1 General overview

Figure 4.1 is a schematic representation of the basic principle of reverse-time migration. The first row shows the building up of the offset-depth-time (x-z-t) cube for a single shot experiment resulting from an impulsive source at point s and time $t = 0$. The front panels correspond to snapshots of the x-z plane; the top panels the x-t plane. As indicated in the figure, part of the top panel in the rightmost cube corresponds to the recorded wavefield.

The second row shows the reconstruction process resulting from the backward propagation in time of two *independent* experiments. In both case the velocity model used in the propagation (background model) is a smooth approximation of the true model, without the sharp contrasts associated with the reflectors. One experiment uses the recorded wavefield as a line source that lies along the positions occupied by the receivers. The other experiment has as initial condition the last snapshot of a forward propagation experiment similar to the actual experiment (i.e., a point source at the source position), but without reflections since it uses a smooth background model.

The limited aperture of the recorded wavefield results in a partial reconstruction in depth of the reflected wavefield as it is propagated back in time. Furthermore, the reversed propagated reflected wavefield does not "die out" in the interface location (not only because of the smooth background velocity but also because of the missing transmitted/converted wavefields). As we overlay simultaneous snapshots of the two experiments, only the points belonging to the interface have nonzero values for both wavefields. Therefore, an image of the reflector can be obtained by summing for all times the product of the wavefields generated by the two experiments.

A similar formulation could be achieved by using a point diffractor instead of an interface, but since we are dealing with plane-wave reflection coefficients, the use of an interface seems to be more appropriate to illustrate the general principle of the method. Up to this point only the kinematics of the method have been analyzed. The next sections also incorporate the dynamics of the migration in the formulation of the imaging principle.

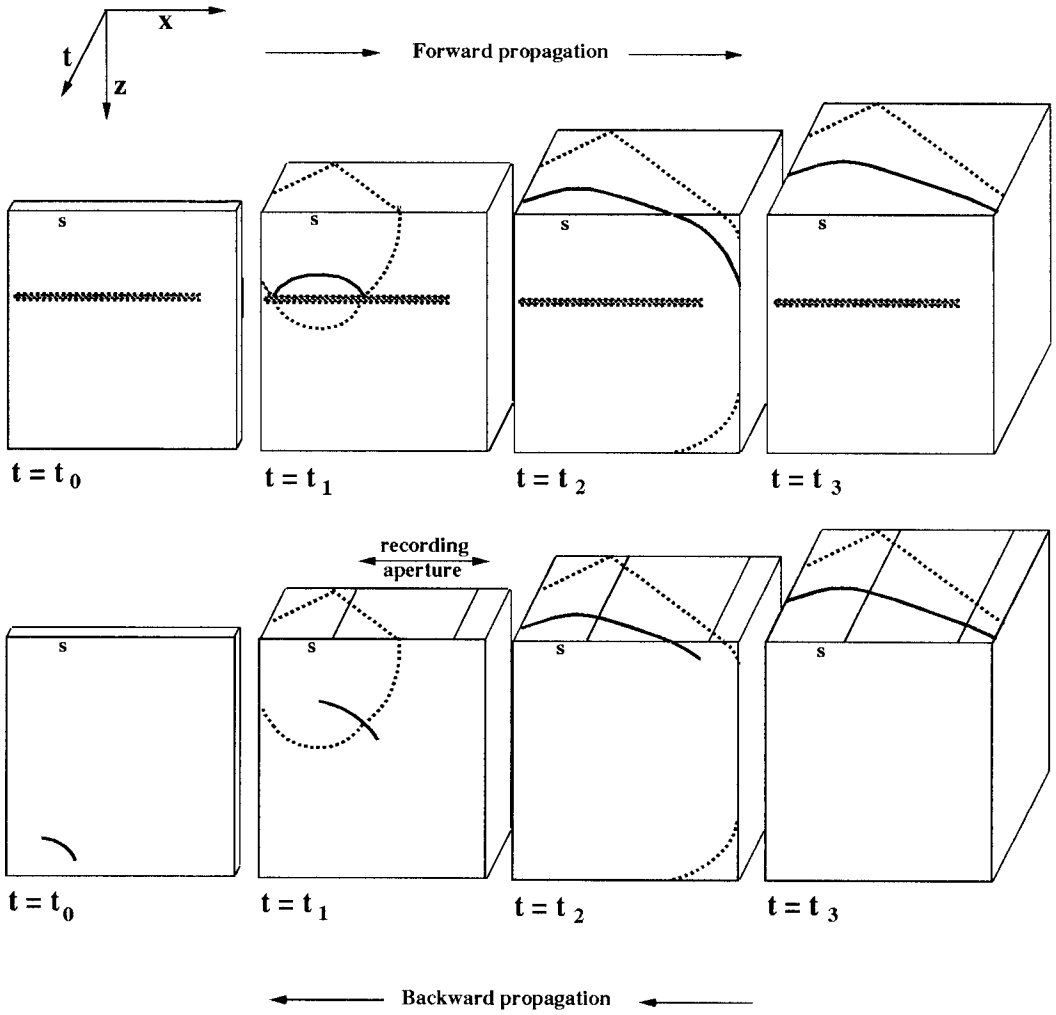

FIG. 4.1. **Top:** Building up of the x-z-t cube during a forward modeling experiment with an impulsive source at s. The model has a single horizontal interface. The front panels show the wavefront expansion in the two-dimensional model space, and the top panels show successive steps in the evolution of the recording space. **Bottom:** Reverse time propagation of the modeled wavefield, with the recorded wavefield added as a source term at the surface, within the region where the receivers are located (two parallel lines in the top panels). The points where the upcoming and downgoing wavefields overlap define the image.

4.2.2 Elastic formulation

The following steps are involved in the elastic reverse-time migration scheme developed in this work:

- Forward modeling of the particle-displacement $\mathbf{u}^{\mathbf{s}}(x,z,t;x_s)$ and particle-velocity $\dot{\mathbf{u}}^{\mathbf{s}}(x,z,t;x_s)$ wavefields, up to the end time of the shot record using the dual-operator elastic modeling described in chapter 3.[1]

- Backward time propagation of the recorded particle-displacement field $\mathbf{u}^{\mathbf{r}}(x,z,t;x_s)$ and its time-derivative $\dot{\mathbf{u}}^{\mathbf{r}}(x,z,t;x_s)$, starting at the end time of the shot record and ending at time zero. These wavefields are introduced as a source term at the receiver locations. The reverse propagation is described by the time reverse of equation (3.13), with the source term replaced by the recorded wavefield $g(x,z=z_r,t;x_s)$, as follows:

$$\begin{pmatrix} \mathbf{u}^{\mathbf{r}} \\ \dot{\mathbf{u}}^{\mathbf{r}} \end{pmatrix}_{t-dt} \approx \mathbf{P}^{-} \begin{pmatrix} \mathbf{u}^{\mathbf{r}} \\ \dot{\mathbf{u}}^{\mathbf{r}} \end{pmatrix}_{t} + \mathbf{B}\,\tilde{\mathbf{g}}, \tag{4.1}$$

  where $\mathbf{B}$ is an operator that depends only on powers of dt, $\tilde{\mathbf{g}} = (\mathbf{g}, \dot{\mathbf{g}}, \ddot{\mathbf{g}}, \ldots)$, and $\mathbf{P}^{-} = \mathbf{P}^{+}(-dt)$.

- Application of the imaging principle.

4.2.3 A single experiment approach

Conventional reverse-time migration (RTM) schemes start with two independent wavefield simulation experiments that are propagated backward in time. One experiment starts with the final result of a forward wavefield simulation using a background model (ideally smooth) that should be a good approximation of the actual model. The other experiment starts with a null wavefield and a source term (located at all receiver positions) that corresponds to the time-reversed recorded wavefield. If the migration is part of a wavefield

[1] Because the imaging step requires access to the time slices generated in this step in the reverse time sequence, this step cannot be performed simultaneously with the imaging step. Since the modeled wavefield cubes are too large to be held in core memory, we are left with two options for solving this problem: to store the cubes in an auxiliary file to be read in reverse order during the imaging step, or to keep only the last time slice and do reverse-time propagation simultaneously with the imaging step. In the scheme presented here, I use the first option not only because it has a better performance but more importantly because the result is not affected by the absorbing boundary or the extra dispersion caused by the backward propagation. Actually, depending on the imaging condition, only the potentials derived from these wavefields are saved for later use.

inversion scheme, the source term in this second experiment is given by the difference between the recorded and the simulated wavefields at the receiver position.

There are other equivalent formulations for RTM depending on how the introduction of the recorded wavefield is interpreted. According to Duhamel's principle (Zauderer, 1989), the solution of an inhomogeneous hyperbolic differential equation can be expressed as the time convolution of the solution of a homogeneous equation, with the inhomogeneous term (the source term) as initial condition. Another formulation introduces the recorded field as a time-dependent boundary condition at the surface (McMechan, 1983). With this formulation, in contrast to the other two, the recorded field is not added to the propagating wavefield at each time step, but instead replaces it at the receiver locations.

Using a variant of the boundary condition formulation, it is possible to design an alternative approach that uses only *one wavefield simulation experiment.* The first step is identical to the first step of conventional RTM methods, that is, forward modeling. During this step the elastic wavefield at all four boundaries of the model is "recorded" for later use. Also, as in conventional RTM schemes, the final wavefield $\mathbf{u}(x, z, t = t_f; x_s)$ is used as initial condition for the reverse-time propagation, but at the boundary grid-points where the receivers are located the back-propagating wavefield is replaced by the recorded wavefield. It is also possible to interpret the replacement of the boundary as the addition of a source term given by the difference between the recorded and back-propagating wavefields as in full wavefield inversion methods (Tarantola, 1986; Mora, 1987). However, this method differs from full wavefield inversion methods in that a time-dependent wavefield is also introduced at all boundaries of the model and no correlation is performed between the backward extrapolated wavefield and a forward extrapolated wavefield to obtain the model perturbation-corrections.

This single-experiment approach offers some advantages over the usual two-experiment methods. First, if the background model coincides with the actual model, then the reverse-propagating wavefield will completely collapse to the point source at time $t = 0$, without the generation of any unwanted multiples in the process. If the background model closely approximates the actual model, then at each interface the backward-propagating reflected, transmitted, and converted wavefields will add up to produce a good approximation of the backward-propagating incident field and a weak scattered field. At each interface, all the wavefields involved in the partitioning process will closely approximate the actual wavefields, with transmission/conversion losses from upper interfaces properly compensated for.

A different imaging criterion (plane-wave-response) is required for these formulation. The next section defines this criterion, and discusses its implication in the correct significance of the final imaging.

4.3 Imaging principle

Migration includes two distinct steps: downward extrapolation in depth or backward extrapolation in time, and imaging for the desired attribute. When the desired attribute is related to the impedance contrasts in the subsurface Claerbout's imaging principle, (Claerbout, 1971) represents the basis for many imaging condition equations. According to this principle, a reflector exists at a point where the upcoming and the downgoing wavefields coincide in time and space. Two distinct factors affect the implementation of this principle: the choice of the specific attribute that we seek to image (*imaging condition*), and the definition of the procedure to be used in the estimation of that attribute (*imaging criterion*).

If the migration is designed with the sole purpose of obtaining a structural image (imaging condition) of the compressional impedance contrasts in the subsurface, then the imaging criterion must be formulated so that it favors noise reduction over amplitude preservation. If, however, the goal is to obtain an image of attributes (imaging condition) that can be correlated to the fluid content of porous rocks, or used as the basic information for a lithological inversion scheme, then the imaging criterion must represent a statistically meaningful estimation of that attribute.

The next section considers the definition of "instantaneous" imaging conditions without addressing the problems of how to deal with stabilization requirements when the amplitude of the incident field is small, or how to do the time average to obtain a meaningful estimation. These two problems are addressed in the section that defines the imaging criterion.

4.3.1 Defining the imaging condition

PP reflection coefficient

In most practical cases only purely compressional modes can be resolved from conventional surface seismic data, especially if the data were collected in a marine environment where

shear waves cannot be generated or recorded. In such cases the only reliable reflection coefficient to image is the one associated with P to P reflections.

Refection coefficients are often defined for either displacement-amplitude ratios or potential ratios. For a pure compressional wave the displacement field can be expressed as the gradient of a potential field. Taking the divergence of the displacement and using the wave-equation for the potential leads to

$$\phi(x,z,\omega) \;=\; \frac{v_p^2}{\omega^2}\,\nabla^2\phi(x,z,\omega) \;=\; \frac{v_p^2}{\omega^2}\,\nabla\cdot\mathbf{u}(x,z,\omega). \tag{4.2}$$

It is clear that the above formulation is restricted to isotropic cases where P waves are described by a single velocity v_p; however the background medium, used for the time extrapolation, is considered to be anisotropic. This means that anisotropic behavior is correctly handled in the propagation through the overburden, but not at the target zone. The displacement reflection coefficient relates to the potential reflection coefficient as follows:

$$\text{Displacement coefficient} \;=\; \frac{v_{inc}}{v_{ref}}\;\text{Potential coefficient},$$

(Aki and Richards, 1980). Since the velocities for the incident and reflected wave are the same, the imaging condition for obtaining the PP displacement reflection coefficient can be formulated as

$$R_{PP}(x,z,t) \;=\; \frac{\phi^r(x,z,t)}{\phi^s(x,z,t)} \;=\; \frac{\nabla\cdot\mathbf{u}^{\mathbf{r}}(x,z,t)}{\nabla\cdot\mathbf{u}^{\mathbf{s}}(x,z,t)}, \tag{4.3}$$

where superscripts r and s correspond, respectively, to the reverse propagated *recorded* wavefield and to the forward propagated *shot* wavefield.

It is important to emphasize that the wavefield decomposition for separating the purely compressional field is performed only at the imaging step, whereas the propagation (depth extrapolation) uses the full wavefield. Thus, all elastic effects of mode conversion in all interfaces are taken into account.

PS and SP reflection coefficients

Similarly, a pure S_v shear mode can be described by the curl of a vector potential. To isolate the shear wave, it is enough to apply a curl operator to the displacement field, as follows:

$$\boldsymbol{\chi}(x,z,\omega) \;=\; \nabla\times\mathbf{u}(x,z,\omega) \;=\; \nabla\times\nabla\times\boldsymbol{\psi}(x,z,\omega), \tag{4.4}$$

For this 2-D implementation the wavefields are invariant in the direction of the unit vector normal to the experiment plane $\hat{\mathbf{y}}$. As a result, the only nonvanishing component of χ is in the $\hat{\mathbf{y}}$ direction. Defining

$$\chi(x,z,\omega) \;=\; (\nabla \times \mathbf{u}(x,z,\omega)) \cdot \hat{\mathbf{y}}$$

and using the same approach as for PP results in the following equations, which describe the imaging condition for the PS reflection coefficient as

$$R_{PS}(x,z,t) \;=\; \frac{v_p\, \chi^r(x,z,t)}{v_s\, \phi^s(x,z,t)} \;=\; \frac{v_s\, (\nabla \times \mathbf{u^r}(x,z,t)) \cdot \hat{\mathbf{y}}}{v_p\, \nabla \cdot \mathbf{u^s}(x,z,t)}, \tag{4.5}$$

and for the SP reflection coefficient as

$$R_{SP}(x,z,t) \;=\; \frac{v_s\, \phi^r(x,z,t)}{v_p\, \chi^s(x,z,t)} \;=\; \frac{v_p\, \nabla \cdot \mathbf{u^r}(x,z,t)}{v_s\, (\nabla \times \mathbf{u^s}(x,z,t)) \cdot \hat{\mathbf{y}}}. \tag{4.6}$$

SS reflection coefficient

The treatment for the SS reflection coefficient is analogous to that for the PS and SP coefficients. The final relation is

$$R_{SS}(x,z,t) \;=\; \frac{\chi^r(x,z,t)}{\chi^s(x,z,t)} \;=\; \frac{(\nabla \times \mathbf{u^r}(x,z,t)) \cdot \hat{\mathbf{y}}}{(\nabla \times \mathbf{u^s}(x,z,t)) \cdot \hat{\mathbf{y}}}. \tag{4.7}$$

Scattering matrix coefficient

For anisotropic media, it is necessary to make the distinction between group and phase properties. The equations relating the several reflection and transmission coefficients with the elastic properties of the medium are derived for plane waves, which imply that the coefficients are associated to ratios between *phase amplitudes.*

One possible approach is to perform a local plane-wave decomposition, integrating the component of the vector-wavefield in the local polarization direction ($\mathbf{j}(x,z,t)$) along different directions p in order to build a function $A(p,x,z,t)$, which represents the phase amplitude for each point of the space-time as a function of the horizontal slowness, and a polarization vector function $\mathbf{j}(x,z,t)$. Time averaging should in this case provide three expectations:$\tilde{A}(x,z)$, $\tilde{p}(x,z)$, and $\tilde{j}(x,z)$. Next we use the Christoffel equation with the background elastic parameters used in the migration to find the wave type associated with each polarization vector. Then an anisotropic inversion scheme can estimate the elastic parameters that best fit the scattering relation involving $\tilde{A}$ for the different modes and $\mathbf{j}$, as a function of the horizontal slowness $\tilde{p}$.

Stiffness perturbations

Most imaging methods described in the literature involve a correlation between scalar wavefields. An exception is the tensorial imaging condition formulated by Karrenbach (1991):

$$\delta c_{jklm}(x,z,t) = \partial_m[\phi_l^s(x,z,t)]\partial_k[\delta\phi_j^r(x,z,t)],$$

where ϕ_l^s is the l component of the forward modeled shot wavefield, and $\delta\phi_j^r$ is the reverse propagated difference between the forward modeled wavefield at the receivers and at the recorded wavefield. This process is equivalent to one step of a wavefield inversion scheme, and δc_{jklm} can be interpreted as the estimated perturbation in the stiffness tensor. In this sense, it can be considered as an extension of Tarantola's (1986) elastic inversion theory to the general anisotropic case.

Hildebrand (1987) used a variation of this principle to image for the acoustic impedance rather than the reflection coefficient, using reverse-time migration to extrapolate the pressure and particle-velocity wavefields. In contrast to the above formulation, Hildebrand's approach obtains an image of the impedance (rather than the perturbations), using a recursive depth-extrapolation procedure.

4.3.2 Defining the imaging criterion

The imaging conditions discussed in the preceding section obtain an estimation of the imaging attribute at a particular point in the four-dimensional (for a 2-D treatment) 2-D space×time×shot-position domain. The imaging criterion defines the statistical approach needed to reduce this information to the expectation value of the attribute in the three-dimensional domain spanned by 2-D space×incidence-angle. There are two major paths for performing this reduction, either

$$data(x_r,t;x_s) \begin{array}{c} \xrightarrow{A} \\ \xrightarrow{A} \end{array} \begin{array}{l} R(x,z,t;x_s) \\ \beta(x,z,t;x_s) \end{array} \begin{array}{c} \xrightarrow{B} \\ \xrightarrow{B} \end{array} \begin{array}{l} R(x,z;x_s) \\ \beta(x,z;x_s) \end{array} \xrightarrow{C} R(x,z,\beta) \qquad (4.8)$$

or

$$data(x_r,t;x_s) \xrightarrow{A} R(x,z,\beta,t;x_s) \xrightarrow{B} R(x,z,\beta;x_s) \xrightarrow{C} R(x,z,\beta). \qquad (4.9)$$

In the first path A represents the depth extrapolation and imaging for time t, B represents the time integration process, and C represents the final search over different shot-gathers to

build the function $R(x, z, \beta)$. In the second path A also represents the depth extrapolation and imaging for time t, B represents the time integration process, and C represents the integration over the shot-point axis. The first path starts with an independent estimation of the attribute and the angle for each shotpoint, while the second obtains at the beginning an estimation of the angular distribution of the attribute for each shotpoint.

Correlation-based criterion

The usual approach for implementing the imaging condition involves the zero-lag correlation between the reverse-propagated recorded wavefield and a function of the reverse-propagated modeled wavefield. The time correlation may also involve a weighting function (or a covariant operator) and a normalization factor. The general form is

$$R(x, z; x_s) = \frac{\int W(x, z, t; x_s)\, \phi^r(x, z, t; x_s)\, F[\phi^s(x, z, t; x_s)]\, dt}{\int W(x, z, t; x_s)\, dt}. \tag{4.10}$$

This criterion is obviously included in the category represented by (4.8), and implicitly requires the use of a smooth background velocity in the wavefield-extrapolation step. Ray-wavefield hybrid methods can be viewed as a particular case of (4.10), with $W = \delta(t - t_s)$, where $t_s = t_s(x, z; x_s)$ is the ray-theoretical traveltime.

Jacobs (1982) compared the implementation of three different forms of equation (4.10), in a prestack profile migration in the ω-x domain:

$$\begin{aligned} R_1 &= \int \phi^r\, [\phi^s]^*\, d\omega, \\ R_2 &= \int \phi^r\, \frac{[\phi^s]^*}{|\,\phi^s\,|}\, d\omega, \\ R_3 &= \int \phi^r\, \frac{[\phi^s]^*}{|\,\phi^s\,|^2 + \epsilon}\, d\omega. \end{aligned}$$

His conclusion was that R_3, though theoretically more correct for estimating the reflection coefficient, was too noise sensitive to be used in that migration scheme. This illustrates the fact that sometimes the imaging condition and the imaging criterion have contradictory requirements: while the former usually involves division by the modeled (incident) wavefield, the latter usually requires multiplication by the same wavefield to assure that only those estimations where the incident wavefield has significant energy will contribute effectively to the final expectation. As emphasized by Claerbout (1992a) the conjugate operation (R_1) is usually more robust than the inverse operation (R_3).

The implementation of the PP reflectivity imaging condition stated in equation (4.3) with the correlation criterion (4.10) uses the following definitions:

$$W(x,z,t;x_s) = [\phi^s]^2(x,z,t;x_s),$$

$$E(x,z;x_s) = \int W(x,z,t;x_s)\,dt,$$

$$F[\phi^s(x,z,t;x_s)] = \frac{1}{\phi^s(x,z,t;x_s)},$$

which result in

$$\begin{aligned} R(x,z;x_s) &= \frac{\int \phi^r(x,z,t;x_s)\phi^s(x,z,t;x_s)\,dt}{E(x,z;x_s)}, \quad \text{where } E(x,z;x_s) \geq E_{cut}(x,z;x_s), \\ R(x,z;x_s) &= \frac{\int \phi^r(x,z,t;x_s)\phi^s(x,z,t;x_s)\,dt}{E_{cut}(x,z;x_s)}, \quad \text{elsewhere,} \end{aligned} \tag{4.11}$$

and the local Snell parameter image as

$$\check{p}(x,z;x_s) = \frac{\int \mid \phi^r(x,z,t;x_s)\,\phi^s(x,z,t;x_s) \mid \tilde{p}(x,z,t;x_s)\,dt}{\int \mid \phi^r(x,z,t;x_s)\,\phi^s(x,z,t;x_s) \mid dt}, \tag{4.12}$$

where $\tilde{p}(x,z,t;x_s)$ is computed from the two wavefields ϕ^r and ϕ^s, as described in appendix A.

In the above equations, $E_{cut}(x,z;x_s)$ is a smooth function that should approximate a fraction of the inverse of the spherical divergence. Equation (4.11) gives the correct estimation of the reflection coefficient in the regions well illuminated by the source ($E(x,z;x_s) \geq E_{cut}(x,z;x_s)$) and a damped estimation in the dim regions.

Figures 4.3 and 4.4 show two images obtained with equations (4.11) and (4.12). The difference between these figures is that a smooth background model was used in the extrapolation step for Figure 4.3 and the original discontinuous model was used in the extrapolation step for Figure 4.4. The source is located 800 meters from the origin and the receivers extend from 980 meters to 2480 meters.

Using a smooth background velocity avoids the contamination of the image by false reflectors caused by reflections in the extrapolation stage. In addition, the two wavefields involved in the migration correspond to unmixed modes (incident and reflected). One disadvantage is that transmission/conversion losses in the interfaces above the target are not compensated for in the extrapolation step. Another disadvantage is the loss in resolution

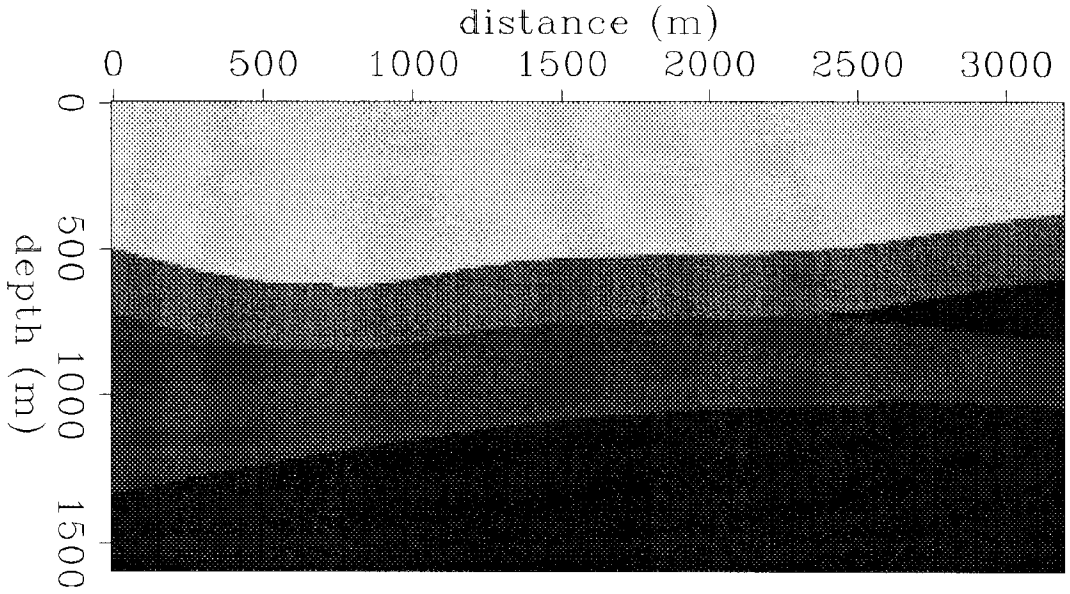

FIG. 4.2. Elastic model used to generate the synthetic profiles that are used to illustrate the different imaging criteria. Only C_{11} is represented in the figure. The model is isotropic; that is, $C_{11} = C_{33}$ for all layers, and the first layer is water ($C_{55} = 0$).

caused by the higher dispersion in the wavefield extrapolation when a smooth background model is used.[2]

When a unsmoothed background model is used in the extrapolation step, the upward propagating modeled field and the downward propagating recorded field can be left out of the imaging computation, but the secondary reflections generated by them will generate false events in the final imaging. Also, at each interface (where the imaging computation is relevant) the two wavefields involved in the migration correspond to a superposition of several modes (incident, reflected, transmitted, and converted), resulting in a contradictory application of the imaging principle. Nevertheless, there are two positive aspects of the use of a discontinuous model. First, the transmission/conversion losses are correctly compensated (at least for the incident wavefield ϕ^s.), and, second, the small dispersion results in a superior resolution.

Figure 4.5 shows the images obtained for the other modes using the correlation criterion implementation of equations (4.5), (4.6), and (4.7). In this figure, both 4.5a and 4.5b refer to the PS reflectivity, but while 4.5a was obtained using the true model, 4.5b was

[2]What I am comparing here is the total dispersion using a model with a few sharp transitions with the total dispersion using a similar model with smooth transitions (but the same contrasts).

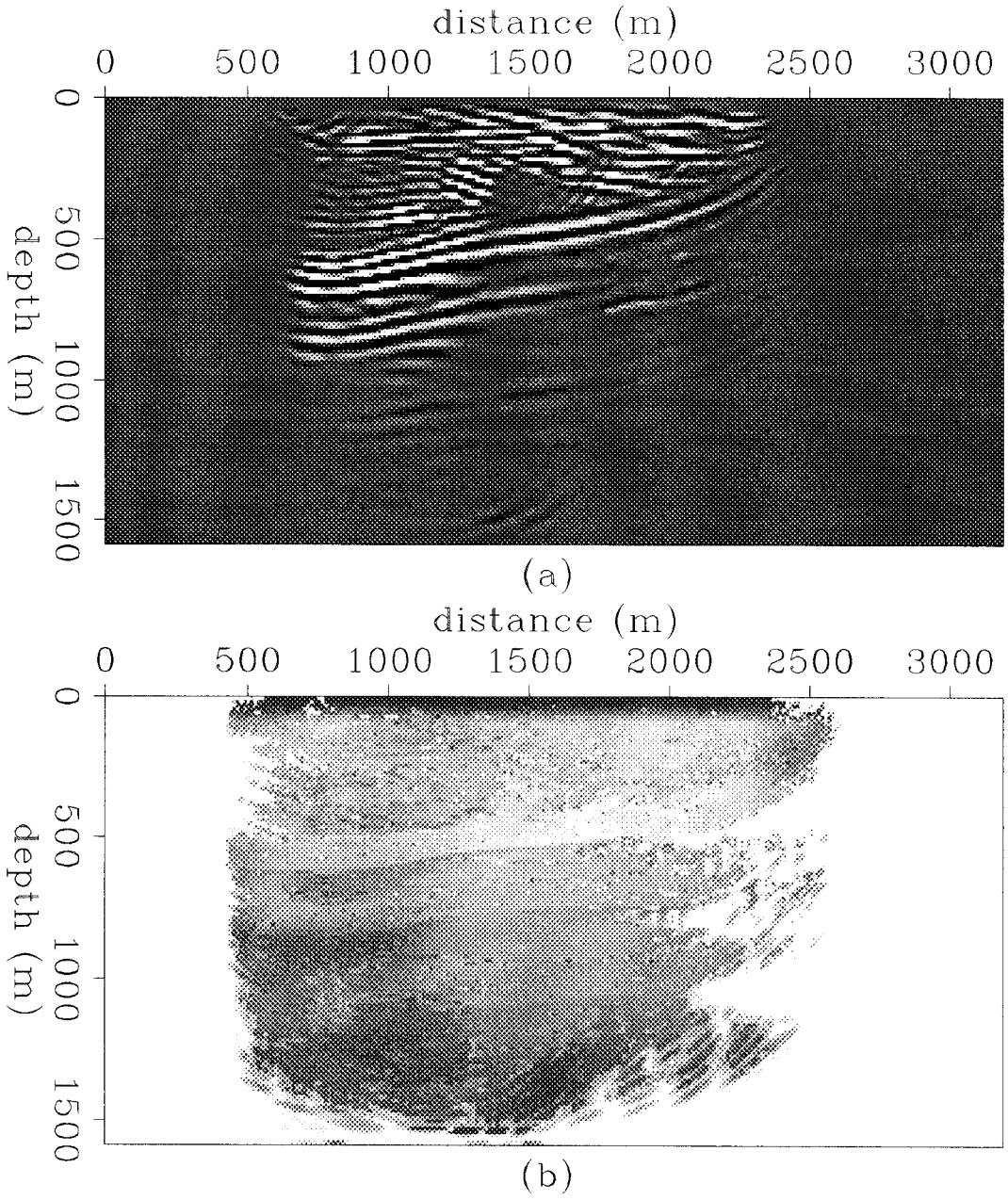

FIG. 4.4. (a) Image of the PP reflection coefficient for a single synthetic shot profile, using the correlation criterion without smoothing the background model. (b) Imaging of the local Snell parameter associated with the reflection-coefficient imaging in (a).

generated using a smoothed model for P velocities and discontinuous (actual) model for S velocities. The other two images, which correspond to SP (4.5c) and SS (4.5d) modes, were also obtained using the true velocity model. All the mode-converted images obtained with a smoothed velocity model were completely unreliable because the mode-conversion dynamics of smooth models are notably different from the mode-conversion dynamics of discontinuous media. Even when the discontinuous model is used, we can see false events that are not related to the generation of multiples, as in the PP case.

Although the ocean floor interface should be absent from all the converted-mode images we can see from the figure that it is actually present in all of them. The reason is that the reverse-propagating P wavefield is partially converted to S in the liquid-solid boundary and the correlation of this converted wavefield with the modeled wavefield (which is also also partially converted to S) produces the false images. These false images of the ocean floor are actually deeper than the PP images because they are formed below the boundary. There are, however, some positive aspects of these converted-mode images. As expected, the regions where the propagation-direction of the wavefield is nearly normal to the interface are not imaged, while some strong reflections can be observed at regions where the incidence angle is large.

V-stack criterion

It is possible to define an imaging criterion that does not produce undesirable false reflections when a discontinuous background model is used. Figure 4.6 shows the modeled wavefield and the reverse propagated recorded field at the same time step. Not only is the incident wavefield reflected and transmitted (only the P wave component is shown), but also the backward-propagated recorded wavefield.

The difference is that, because of its limited aperture, the reflections originating from the reverse propagation of the recorded wavefield will be limited to a small region of space. As illustrated in the same figure, the product of the two wavefields has a peculiar **V** shape with vertex at the reflector. Figure 4.7 illustrates this concept for a synthetic shot profile.

The application of this imaging criterion is not straightforward. The following steps can be used to implement the V-stack criterion:

- Define the product function Ψ^{rs} as

$$\Psi^{rs}(x,z,t;x_s) \;=\; \phi^{r}(x,z,t;x_s)\,\phi^{s}(x,z,t;x_s)$$

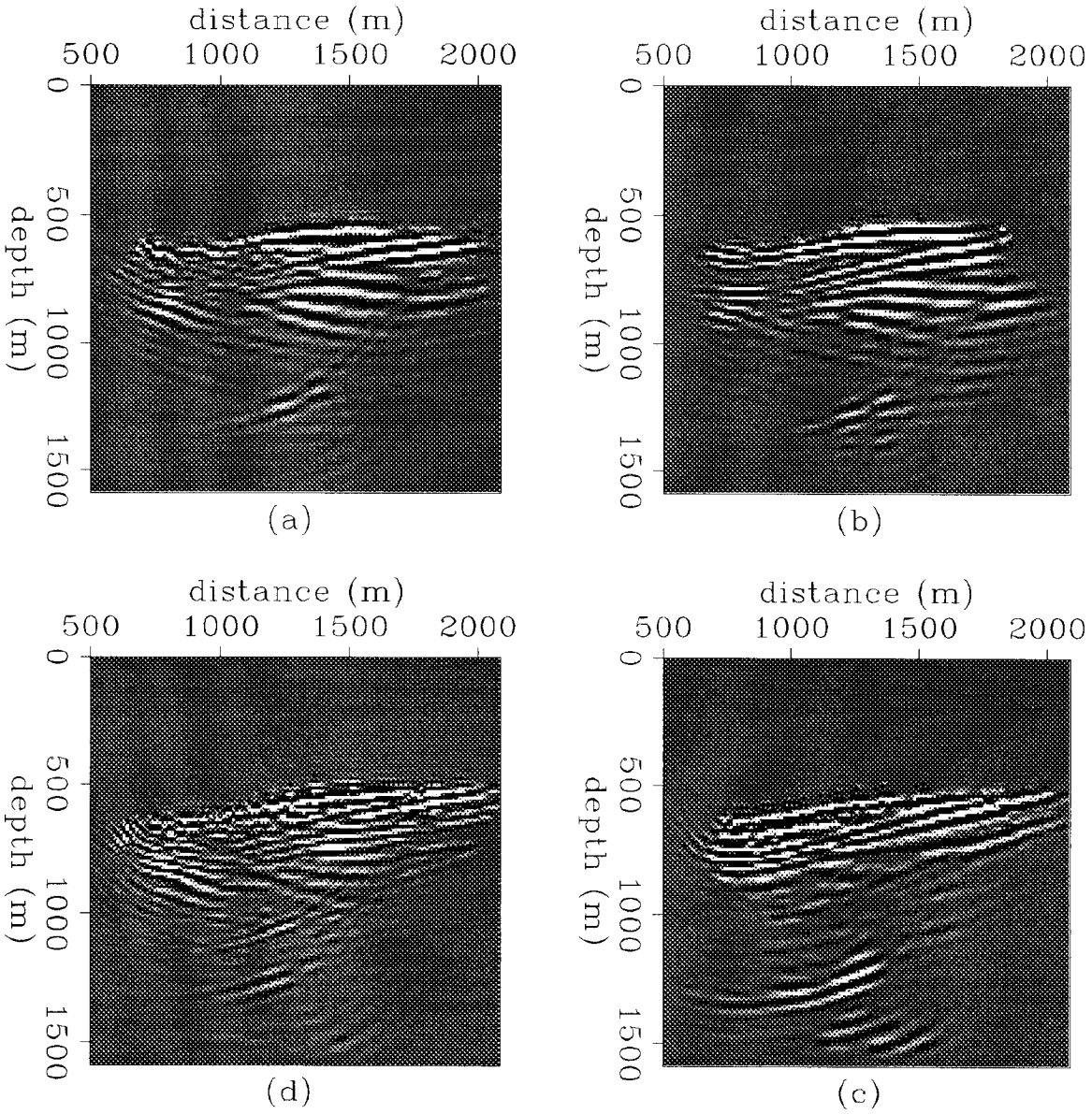

FIG. 4.5. Images of the PS, SP, and SS reflection coefficients for the synthetic gather shown in Figure 4.3. (a) PS reflectivity using the unsmoothed velocity model. (b) PS reflectivity using a smoothed P velocity and the unsmoothed S velocity. (c) SP reflectivity using the unsmoothed velocity model. (d) SS reflectivity using the unsmoothed velocity model.

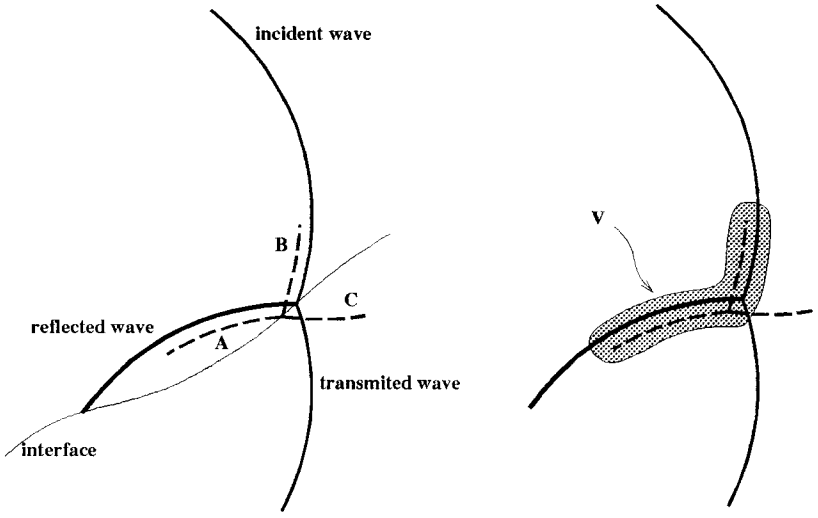

FIG. 4.6. **Right:** The **continuous** thick line represents the modeled wavefield ϕ^s, which is reflected and transmitted at the interface of a discontinuous background model. The **dashed** line represents the backward propagated recorded wavefield ϕ^r with an incident part **A**, which is also reflected **B** and transmitted **C** at the interface. **Left:** The overlapping region of both wavefields define a region with a characteristic "V" shape.

- Calculate the local semblance of Ψ along all directions (θ) around every point (x, z) of the profile x_s as follows:

$$\text{Semb}[\Psi(x,z,t,\theta;x_s)] = \frac{\left[\int_0^{\Delta l} \Psi^{rs}(x + l\cos\theta, z + l\sin\theta, t, x_s)\, dl\right]^2}{\int_0^{\Delta l}[\Psi^{rs}(x + l\cos\theta, z + l\sin\theta, t, x_s)]^2\, dl},$$

  where Δl is the size of the local stacking segment.

- Find the two directions θ_s and θ_r for which Semb[Ψ] is maximum.

- The estimation of the reflection coefficient is given by

$$R(x,z;x_s) = \frac{\int \left[\int_0^{\Delta l} \phi_r(x + l\cos\theta_r, z + l\sin\theta_r, t; x_s)\, dl \int_0^{\Delta l} \phi^s(x + l\cos\theta_s, z + l\sin\theta_s)\, dl\right] dt}{\int \left[\int_0^{\Delta l} \phi^s(x + l\cos\theta_s, z + l\sin\theta_s)\, dl\right]^2 dt},$$

where $\beta = \dfrac{\pi - |\,\theta_s - \theta_r\,|}{2}$ is the angle of incidence.

This criterion offers two advantages for the case of unsmoothed backgrounds relative to the correlation criterion. It will not have spurious events caused by the overlap of secondary reflections, and the attribute is estimated from wavefield contributions away from the interface, where the interference with other modes is much weaker. The next criterion has the same advantages.

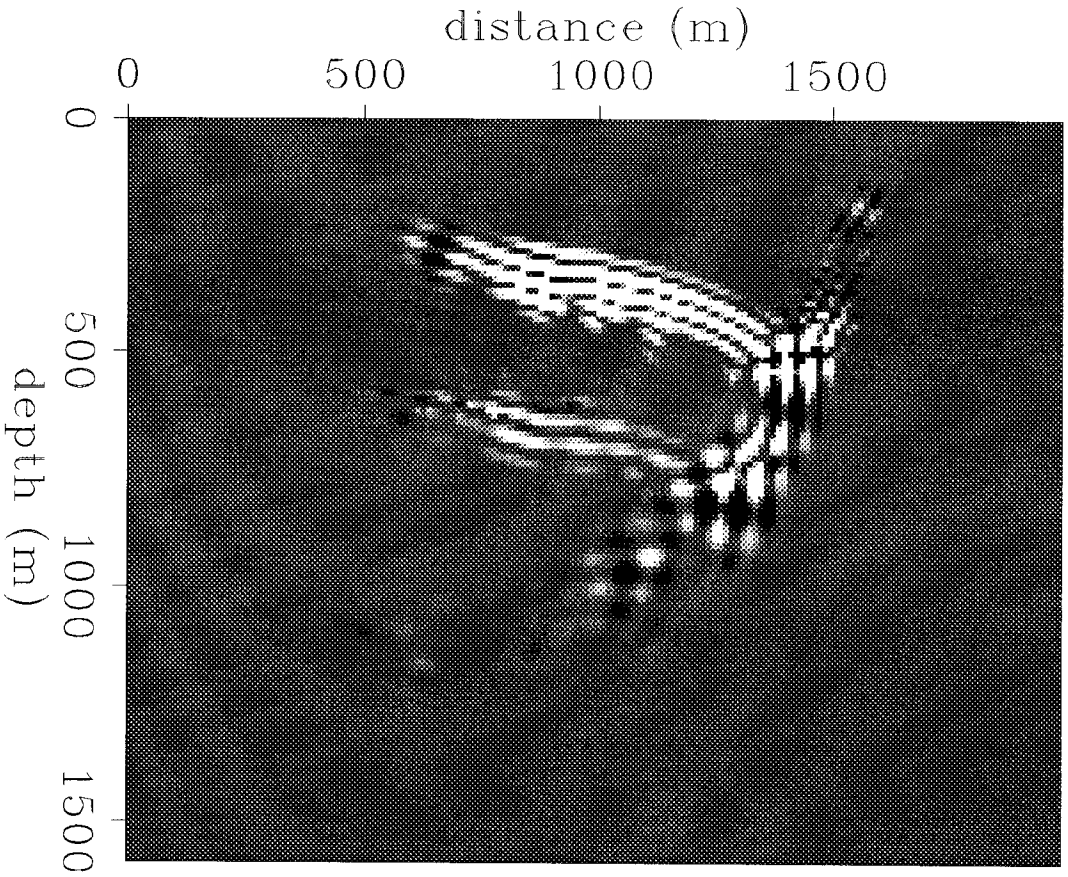

FIG. 4.7. Product of the modeled wavefield ϕ^s and the backward-propagated wavefield ϕ^r for a particular time t when the wavefields intercept two interfaces of the background model. Two V-shaped regions, whose vertex indicates the point of the interface where the wavefield partition takes place, can be observed in the figure.

Plane-wave-response criterion

The relevance of obtaining an estimation of the several angle-dependent reflection coefficients is the prospect of later using this information in a Zoeppritz-based elastic inversion. However, since the Zoeppritz equations represent the plane-wave response of a planar interface, it is necessary that the reflectivity estimation also represent the *in situ* plane-wave response of the interface.

Among the previous criteria, only the V-stack represents a reasonable approximation to this requirement. To obtain an estimation completely consistent with the plane-wave response, it is necessary to perform a complete plane-wave decomposition of the upward and downward propagating wavefields at each point of the model, for all time steps. Although this criterion can be applied to general RTM schemes, it is particularly appropriate for the *one-experiment* approach described before, where a single wavefield (with combined information from the modeled and recorded wavefields) is backward propagated in time, using a discontinuous background model.

The plane-wave-response criterion for the one-experiment RTM scheme is implemented by performing the following steps:

- First, it is necessary to separate the compressional and shear components of the backward extrapolated wavefield. This is done by applying the divergence and rotational operators multiplied by a velocity-dependent term, as indicated in the numerator of equations (4.5) and (4.6), which generates the P and S potentials.

- In the second step , the downgoing $\phi^d(x,z,t;x_s)$ and upcoming $\phi^u(x,z,t;x_s)$ components of each potential are separated using the propagation-direction unit vector $\hat{\mathbf{k}}(x,z,t;x_s) = (k_x,k_z)$ as follows:

$$\begin{aligned} \phi^d(x,z,t;x_s) &= \phi(x,z,t;x_s), && \text{where } k_z < 0 \\ \phi^u(x,z,t;x_s) &= \phi(x,z,t;x_s), && \text{elsewhere.} \end{aligned}$$

  Appendix A describes how to obtain the propagation direction from the field potentials. The downgoing field (within the forward-time reference system) includes the incident and transmitted wavefields, while the upcoming field contains only the reflections.[3] Figure 4.8 shows the estimated propagation directions overlaid on the

[3] Overturning waves are not considered in this analysis.

wavefield, and Figure 4.9 shows the resulting upcoming and downgoing separated wavefields.

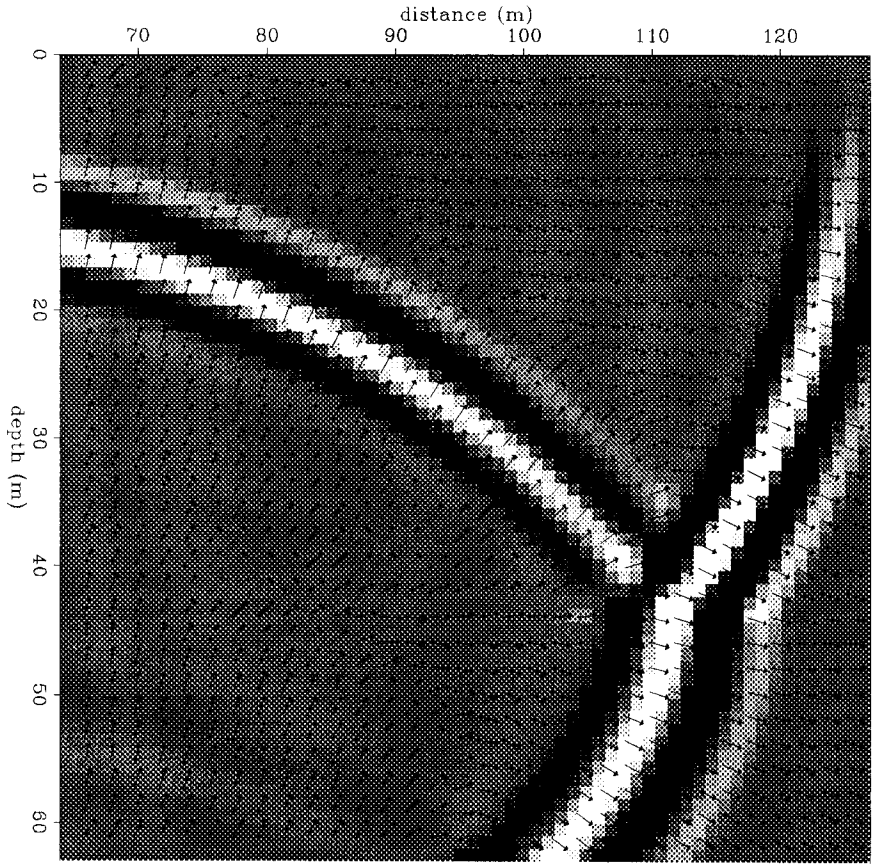

FIG. 4.8. Wavefield partition at an interface. The incident and transmitted wavefields propagate downward, while the reflected wavefield propagates upward. The overlaid arrows indicate the local propagation direction estimated from the wavefield, as described in appendix A.

- The third step involves the computation of the stacking power of the two potentials ϕ^d and ϕ^u (for both P and S wavefields) along the directions represented by the angle θ around each point of the model, as follows:

$$\Phi^d(x,z,t,\theta;x_s) = \int_0^\infty \phi^d(x+l\cos\theta, z+l\sin\theta, t, x_s)\, dl \quad \text{for} \quad 0 \leq \theta \leq 2\pi \tag{4.13}$$

$$\Phi^u(x,z,t,\theta;x_s) = \int_0^\infty \phi^u(x+l\cos\theta, z+l\sin\theta, t, x_s)\, dl. \quad \text{for} \quad 0 \leq \theta \leq 2\pi. \tag{4.14}$$

As in the V-stack case, the stacking power is computed outward from the image point

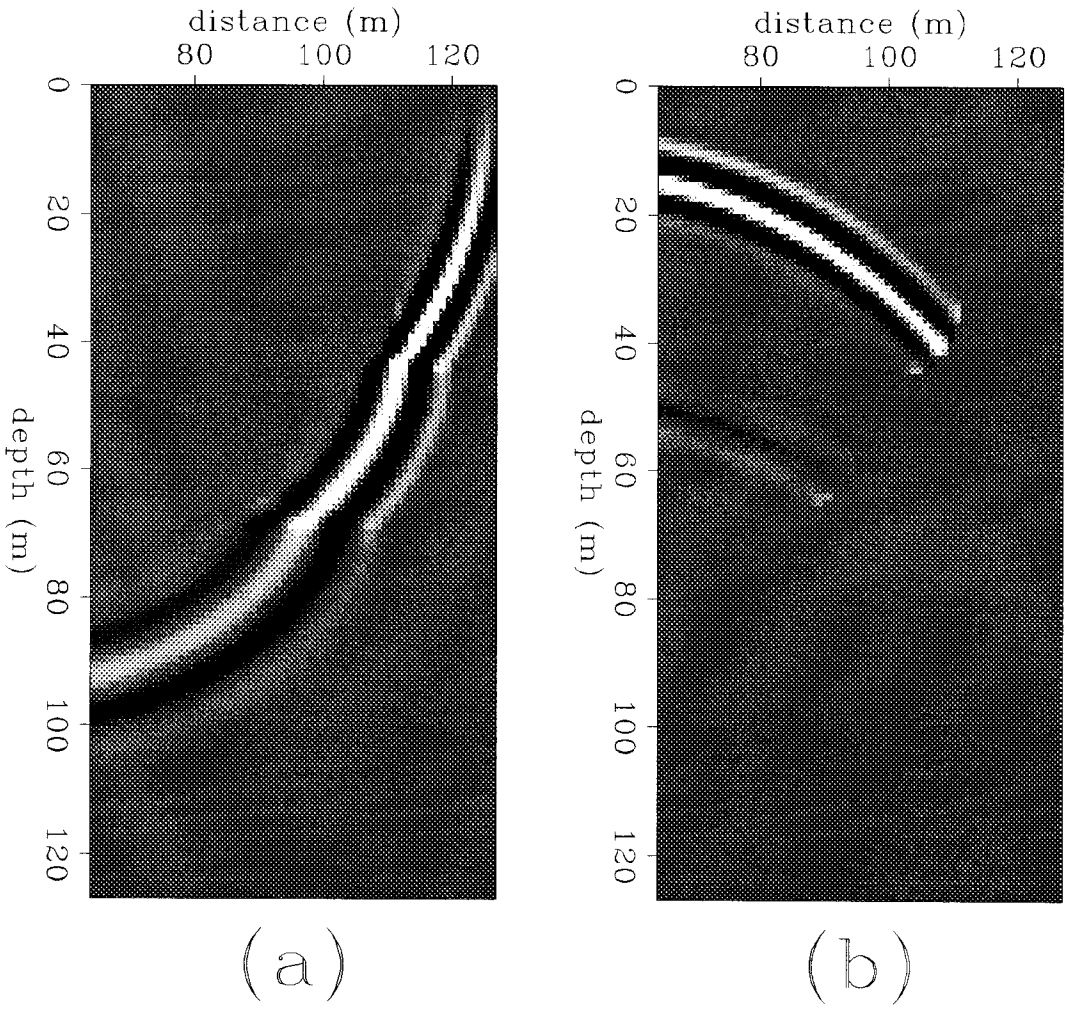

FIG. 4.9. Separation of the upward-propagating and downward-propagating parts of a wavefield, using the local propagation direction. (a) The downward-propagating part corresponding to the incident and transmitted wavefields. (b) The upward-propagating part corresponding to the reflected wavefields.

(stacking trajectories are like a clock's hand), instead of across it. This implies that $\Phi^d(\theta) \neq \Phi^d(\theta + \pi)$. As discussed in appendix B, the point of a given interface that intersects the downgoing wavefield at time t (reflection point) has two directions θ (almost opposite) for which the Φ^d has a local maximum, corresponding to the incident and transmitted waves, but only one direction for which the Φ^u is maximum.

- Evaluate the angle θ^u_{max} for which Φ^u is maximum. For reasons discussed in appendix B this angle determines the subdomain $\Delta\theta(\theta^u_{max})$ in which the correlation between the two stacking power functions is to be evaluated.

- Next, the crosscorrelation $\mathcal{C}$ of the two stacking powers, and the autocorrelation $\mathcal{A}$ of the stacking power of the downgoing wavefield are evaluated, in the interval $\Delta\theta(\theta^u_{max})$, for points $(x, z, t; x_s)$ where $-\frac{\pi}{2} \leq \theta^u_{max} \leq \frac{\pi}{2}$, as follows:

$$\begin{aligned} \mathcal{C}(x,z,t,\beta;x_s) &= \int_{\frac{\pi}{2}}^{\frac{3\pi}{2}} \Phi^u(x,z,t,\theta-\pi+2\beta;x_s)\,\Phi^d(x,z,t,\theta;x_s)\,d\theta \\ \mathcal{A}(x,z,t,\beta;x_s) &= \int_{\frac{\pi}{2}}^{\frac{3\pi}{2}} \Phi^d(x,z,t,\theta;x_s)\,\Phi^d(x,z,t,\theta;x_s)\,d\theta, \end{aligned} \tag{4.15}$$

and for points $(x, z, t; x_s)$ where $\frac{\pi}{2} \leq \theta^u_{max} \leq \frac{3\pi}{2}$, as follows:

$$\begin{aligned} \mathcal{C}(x,z,t,\beta;x_s) &= \int_{-\frac{\pi}{2}}^{\frac{\pi}{2}} \Phi^u(x,z,t,\theta+\pi-2\beta;x_s)\,\Phi^d(x,z,t,\theta;x_s)\,d\theta \\ \mathcal{A}(x,z,t,\beta;x_s) &= \int_{-\frac{\pi}{2}}^{\frac{\pi}{2}} \Phi^d(x,z,t,\theta;x_s)\,\Phi^d(x,z,t,\theta;x_s)\,d\theta. \end{aligned} \tag{4.16}$$

where β is the reflection angle.

- The estimated attributes are given by

$$\begin{aligned} R(x,z,\beta) &= \frac{\int\int \mathcal{C}(x,z,t,\beta_{\max};x_s)\,dt\,dx_s}{E(x,z,\beta)}, \quad \text{where } E(x,z,\beta) \geq E_{cut}(x,z,\beta), \\ R(x,z,\beta) &= \frac{\int\int \mathcal{C}(x,z,t,\beta_{\max};x_s)\,dt\,dx_s}{E_{cut}(x,z,\beta)}, \quad \text{elsewhere,} \end{aligned} \tag{4.17}$$

where

$$E(x,z,\beta) = \int\int \mathcal{A}(x,z,t,\beta_{\max};x_s)\,dt\,dx_s,$$

and $\beta_{\max} = \beta_{\max}(x, z, t; x_s)$ is the angle β for which the absolute value of $\mathcal{C}$ is maximum, that is:

$$|\mathcal{C}(x, z, t, \beta_{\max})| = \max_{\beta} |\mathcal{C}(x, z, t, \beta; x_s)|$$

To obtain R_{PP} we use $\mathcal{C}_{PP}$ and $\mathcal{A}_{PP}$, to obtain R_{SS} we use $\mathcal{C}_{SS}$ and $\mathcal{A}_{SS}$, to obtain R_{PS} we use $\mathcal{C}_{PS}$ and $\mathcal{A}_{PP}$, and to obtain R_{SP} we use $\mathcal{C}_{PS}$ and $\mathcal{A}_{SS}$.

There are two important implementation issues in equation (4.17) that require some clarification. First, instead of integrate over angle (at each time-step) the images obtained for the several angles of incidence only the images corresponding to angles for which the correlation power is maximum (for each model position) is selected. Second, instead of computing $R_{PP}(x, z, \beta; x_s)$ and integrate (average) over the shotpoint axis, it first integrate the crosscorrelation and autocorrelation over the shotpoint axis and then takes the ratio between them to obtain $R_{PP}(x, z, \beta)$.

Figure 4.10 shows the twelve images obtained over a small time window centered at the time-frame of Figure 4.8. Each of these images corresponds to $R(x, z, \beta; x_s)$ at a different local angle of incidence β. The ray-theoretical values for the angle of incidence of the wavefronts that reach the two interfaces at that particular time are 48 degrees for the upper interface and 30.5 degrees for the bottom interface. From the figure it is clear that the point of the upper interface that is imaged at this time has maximum energy at the frames corresponding to 45 and 52.5 degrees, while for the bottom interface the maximum occurs at 30 and 37.5 degrees. Though special care is required to avoid the undesirable focusing at small angles that we observe in the figure, it is encouraging to see that the location of the main maxima are consistent with the expected values. The next section discusses the failure of the PWR imaging condition (as formulated here) for near-normal incidence, and shows how to solve the problem with the introduction of an angle-dependent time shift between the downgoing and upcoming wavefields.

4.4 The plane-wave-response (PWR) migration

The plane-wave-response (PWR) migration combines the one-experiment downward extrapolation approach with the plane-wave-response imaging condition. The one-experiment

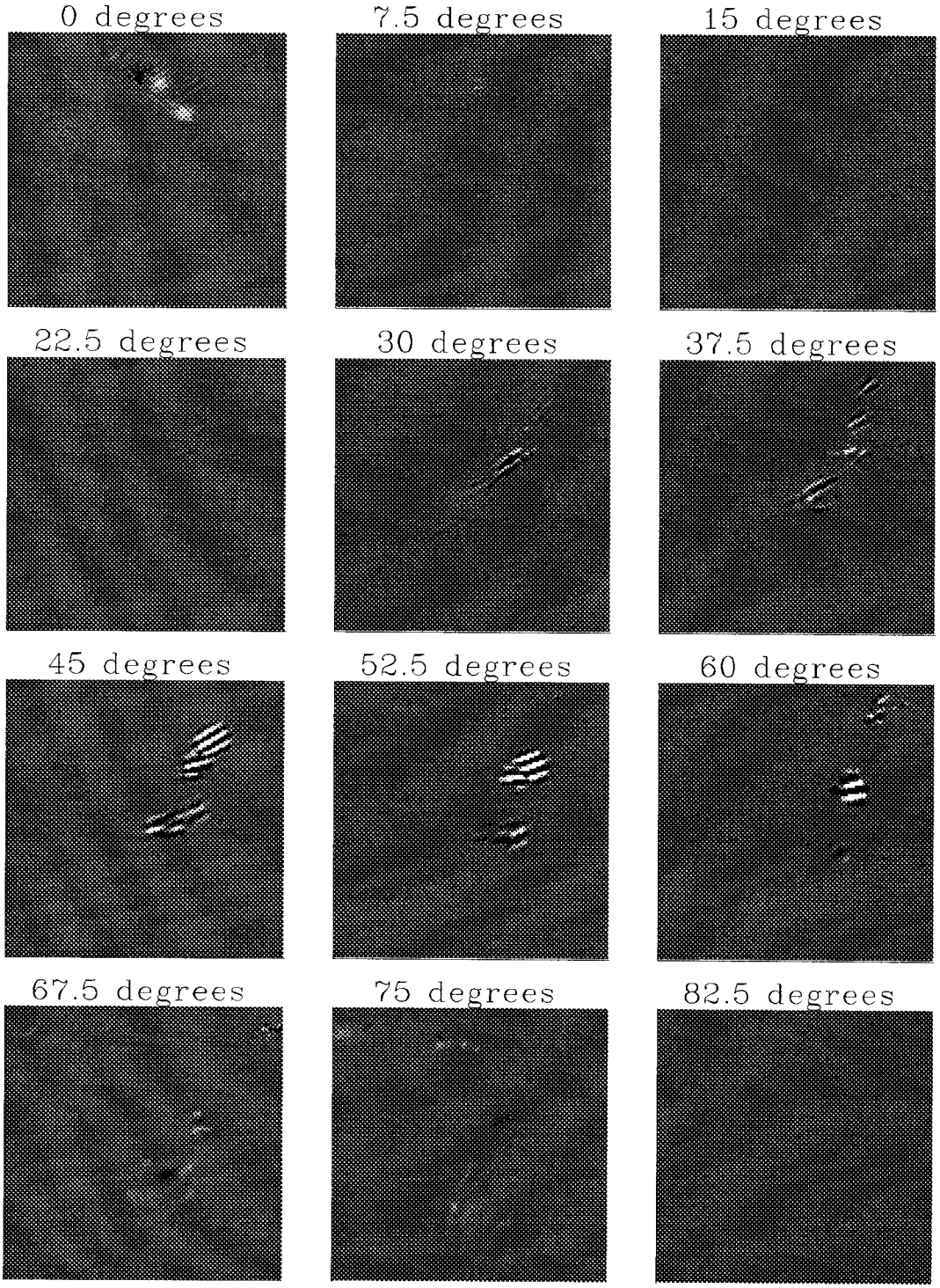

FIG. 4.10. PP reflectivity for a small (6 time steps) time window of the wavefield in Figure 4.8, for different values of the angle of incidence β.

approach to downward extrapolate the recorded wavefield can (assuming a perfect background model) reconstruct the *true-amplitude* wavefields at each time step of the backward-propagation process. When applied to these downward-continued wavefields, the PWR imaging condition generates four images that correspond to the "local plane-wave responses" at each position of the model. To define more precisely what I mean by "local plane-wave responses" it is necessary first to state the assumptions on the elastic model for which this definition applies. The model is considered to be a superposition of homogeneous layers of variable shape and thickness, with the additional constraint that the interfaces between layers are sufficiently smooth to be approximated by a plane within the Fresnel zone of the local wavefield. For a particular point of a given interface, the *local plane-wave responses* are defined as the P and S plane wave responses of a model for which the half-space above the interface is replaced by the layer that overlays the interface at that point.

As observed in Figure 4.10 the *static* formulation of the PWR imaging condition does not give the desired response at small angles of incidence. The cause of the failure lies in the selection of the two wavefields involved in the evaluation of $\mathcal{C}$ in equations (4.15) and (4.16) at the same time-step t. According to Claerbout (1992b) "two plane waves with different slopes should be orthogonal if one of them has zero mean". Because at normal and tangential incidence the incident and reflected plane waves have the same slope they lose their orthogonality, and therefore their separability. Moreover, the mask function criterion used to separate the upward and downward propagating waves favors the strongest wavefield at the regions where the two waves overlap. At intermediate angles of incidence the overlapping regions have a small contribution to the integrals in 4.13 and 4.14, but near normal or tangential incidence these regions have a major contributions to those integrals. It is important to observe that this problems are related only to PP or SS responses not only because PS and SP are easily separable, but also because the response of these converted modes vanishes at normal incidence.

4.4.1 Introducing a time delay in the PWR imaging condition

One solution to the non-orthogonality of incident and reflected plane waves near normal and tangential incidence would be the application of the ω-κ_x domain method described in chapter 2. However, this solution is not compatible with the time-domain extrapolation method in which the PWR migration is based. Another solution, devised for the time

domain, is to introduce a time-delay between the two wavefields correlated (in angle) in equations (4.15) and (4.16).

Figure 4.11 shows an incident wavefield $\phi^d(t)$ at normal incidence at time t, and a reflected wavefield $\phi^u(t+\tau)$ at a later time $t+\tau$. The definition of the time-delay τ is not rigid, but should represent a measure of the "effective period" of the source wavelet, that is, the time interval between the first and last representative samples of the source wavelet. This time-delay guarantees that at the time when the correlation between the two wavefield is maximum (the particular case shown in Figure 4.11) there is no overlapping between the upcoming and downgoing waves. Also shown in the figure is the spatial shift ΔL of the zero-lag of the imaging-wavelet relative to the actual reflection-point. This spatial shift is given by

$$\Delta L \;=\; v\,\frac{\tau}{2}, \tag{4.18}$$

where v is the propagation velocity of the particular wavetype in the upper medium. Since the spatial shift is proportional to τ it is important to make τ as short as possible to avoid a large displacement of the reflector but sufficiently large to avoid the wavefield overlapping when the correlation is maximum.

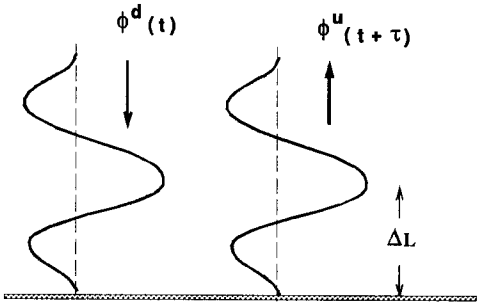

FIG. 4.11. Incident wavefield at time t and reflected wavefield at time $t+\tau$ for the case of normal incidence to the reflector's plane. The time delay τ is equal to the "effective period" of the source wavelet.

To guarantee that the zero-lag of the imaging-wavelet is always located at the same position above the reflection-point for all illumination angles β, it is necessary to define an angle-dependent time delay $\Delta t(\beta)$ such that $\Delta t(0) \;=\; \tau$. Figure 4.12 shows an incident plane wave $\phi^d(t)$ at time t (bold lines), the reflected plane wave $\phi^u(t)$ at the same time step (thin lines), and the zero-lag wavefront of the delayed reflected plane wave $\phi^u(t+\Delta t)$ (normal line), for the case of non-normal incidence.

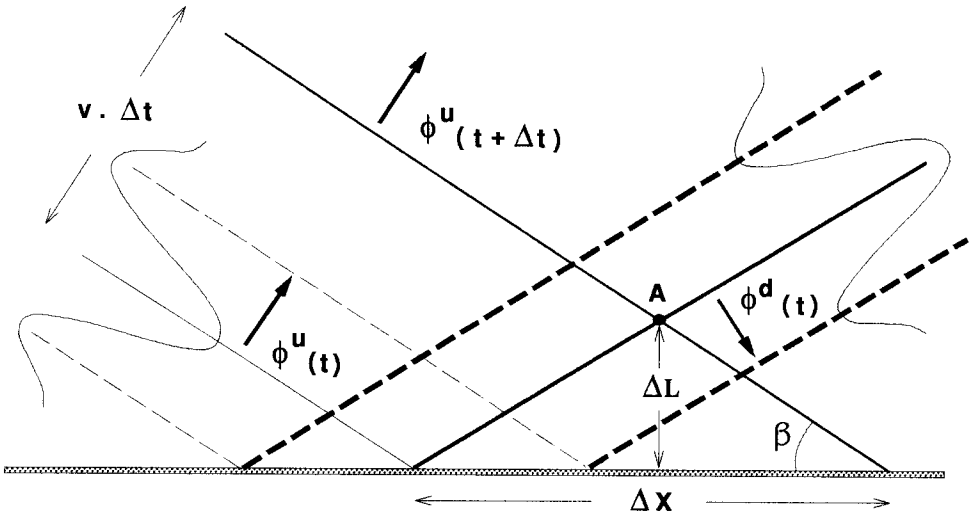

FIG. 4.12. Incident wavefield at time t, reflected wavefield at time t, and reflected wavefield at time $t + \Delta t$, for the case of non-normal incidence. The time delay Δt is such that the distance ΔL between the interception point A (between the central pick of the incident and reflected wavefields) is equal to the normal incidence distance.

From the figure we obtain the relations

$$\Delta x \;=\; \frac{v\,\Delta t}{\sin(\beta)}$$

and

$$\tan(\beta) \;=\; \frac{2\,\Delta L}{\Delta x},$$

which can be combined to give

$$\Delta t \;=\; \frac{2\,\cos(\beta)\,\Delta L}{v}.$$

Since ΔL must be the same for all angles, we can substitute the normal-incidence relation 4.18 into the previous equation to obtain the time-delay function

$$\Delta t \;=\; \tau\,\cos(\beta). \tag{4.19}$$

The inconvenience for introducing the angle-dependent time delay in the imaging condition is the required increase in the allocation of in-core memory. The implications of this "collateral effect" are discussed later in the chapter.

With this new dynamic formulation the crosscorrelation part of equations (4.15) and (4.16) become, for points $(x,z,t;x_s)$ where $-\frac{\pi}{2} \le \theta^u_{max} \le \frac{\pi}{2}$,

$$\mathcal{C}(x,z,t,\beta;x_s) = \int_{\frac{\pi}{2}}^{\frac{3\pi}{2}} \Phi^u(x,z,t+\tau\cos(\beta),\theta-\pi+2\beta;x_s)\,\Phi^d(x,z,t,\theta;x_s)\,d\theta, \tag{4.20}$$

and for points $(x,z,t;x_s)$ where $\frac{\pi}{2} \le \theta^u_{max} \le \frac{3\pi}{2}$

$$\mathcal{C}(x,z,t,\beta;x_s) = \int_{-\frac{\pi}{2}}^{\frac{\pi}{2}} \Phi^u(x,z,t+\tau\cos(\beta),\theta+\pi-2\beta;x_s)\,\Phi^d(x,z,t,\theta;x_s)\,d\theta. \tag{4.21}$$

4.4.2 An outline of the PWR migration

The PWR migration can be summarized as follows:

1. Forward time propagation using an estimation of the actual source radiation pattern as the source term, absorbing boundaries at the sides and the bottom, free surface boundary at the top, and an unsmoothed elastic background model. At each time step the elastic displacement field and its time-derivative, at the three boundaries between the absorbing and non-absorbing regions as well as at the horizontal row in which the cable is located, are stored for later use. The complete wavefield and its time-derivative at the last time frame are also saved for use in the next stage.

2. Backward time propagation using the wavefields saved at the previous stage as time-dependent boundary conditions. At the model points where the receivers are located, the boundary-condition-wavefields are replaced by the recorded wavefield. At each time-step of this stage:

   - Apply the divergence and rotational operators to the backward-propagated displacement-field to obtain, respectively, the P-wave potential and the S-wave potential.
   - For each potential, estimate the propagation-direction field and based on the sign of its vertical component separate the downward and upward propagating potential fields.
   - For each potential, calculate the downward and upward propagating plane-wave components for all angles β. A record of the last τ/dt time steps must be kept updated.
   - Using the classification criteria described in appendix B, apply equations (4.20) and (4.21) to obtain, for each angle of incidence β, the autocorrelation $\mathcal{A}(\beta)$ and crosscorrelation $\mathcal{C}(\beta)$. These calculations involve the downgoing potential at the present time-step t and the upcoming potential at the time-step $t+\Delta t(\beta)$.
   - Sum over time, for each model point, the value $\mathcal{C}$ and $\mathcal{A}$ corresponding to the angle for which $\mathcal{C}(\beta)$ is maximum, to obtain the time integrals in the numerator and denominator of equation (4.17).

3. Sum over all the shotpoints, the time integrals of $\mathcal{C}$ and $\mathcal{A}$ and apply equation (4.17) to obtain the four image-cubes.

4.4.3 Application of the PWR migration to synthetic data

To test the resolution of the method for retrieving the plane-wave reflection coefficient, I applied the PWD migration to the three-layer model used to test the modeling schemes in chapter 3 (see Figure 3.9). Figure 4.13 shows some frames of the crosscorrelation cube $\mathcal{C}(x, z, \beta; x_s)$, which corresponds to the numerator of equation 4.17 after the integration over time but before the integration over shotpoint. Each panel corresponds to a different angle of incidence of a plane wave relative to the local reflector normal. Because the model is comprised of horizontal layers, the horizontal coordinate in each panel can be interpreted

either as different subsurface positions for a fixed shotpoint, or as different shotpoints for a fixed subsurface position. For the fixed-shotpoint interpretation, the source is located at the upper-left corner of each frame. As expected, at 0 degrees only the points below the source are imaged, and as the incidence-angle increases, the imaged-point moves to the right. Because the background is not homogeneous, the two image-points are not aligned radially from the source. The apparent artifacts at 22.5 and 30 degrees are actually images associated with a multiple reflection. Multiples are imaged at the right position and angle; therefore, instead of degrading the image (as it usually happens) they actually improve the estimation of the reflectivity.

Figure 4.14 shows the result of integrating the crosscorrelation cube of Figure 4.13 over shotpoint and dividing by the associated integral of the autocorrelation cube, as described by Equation (4.17). This figure corresponds to an estimation of the plane-wave reflectivity function for a given column of the model. Figures 4.15 and 4.16 compare the estimated reflectivity functions of the two interfaces with the analytical functions. Although the fitting is not perfect, the angular behavior of the estimated response is similar to the angular behavior of the analytical curve.

4.4.4 Discussion

The results obtained by the PWR migration in synthetic data support the theoretical formulation of the method. The errors in the retrieval of the plane-wave reflectivity are within the limits imposed by the theory and by the implementation process. Next, I discuss the present theoretical and practical limitations of the method as well as some directions for future development.

The major practical limitation resides in the excessive in-core memory allocation required for storaging the delayed upcoming plane-wave field. Since this four-dimensional array is accessed in the innermost loop of the algorithm it is not plausible to use out-of-core allocation; computation time would become excessively high.

Because of the memory limitation and also because the computation cost is proportional to the number of angles involved, the angular coverage has to be sparse. With the available hardware resources I was limited in the synthetic examples of this chapter and in the field data examples of chapter 5 to a maximum coverage of 24 propagation angles, which implies a resolution of 15 degrees in the plane-wave decomposition. This restriction affects not only the final angular resolution of the reflectivity function (7.5 degrees) but

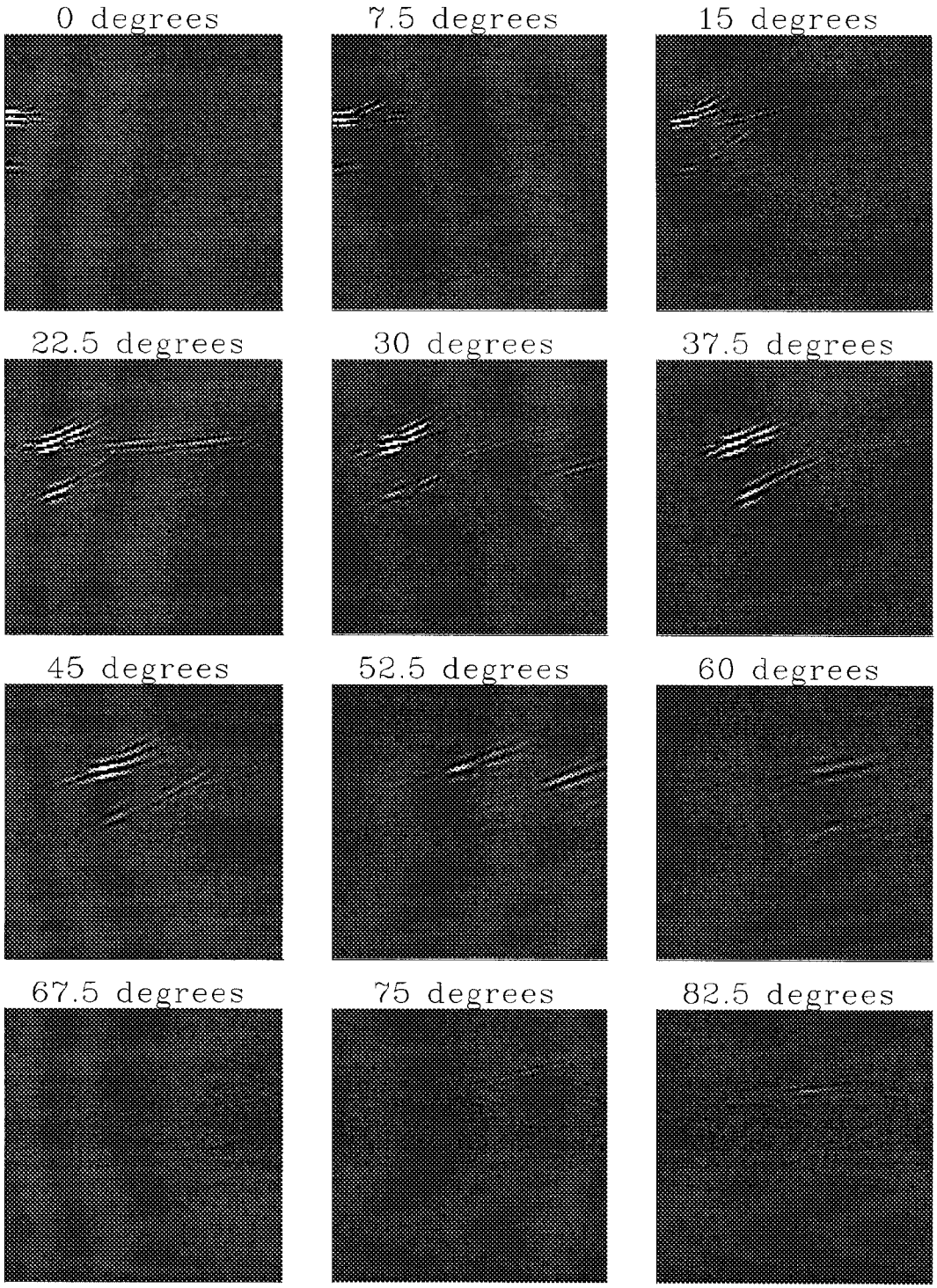

FIG. 4.13. PP crosscorrelation cube (before integration over shotpoint) for the model of Figure 3.9.

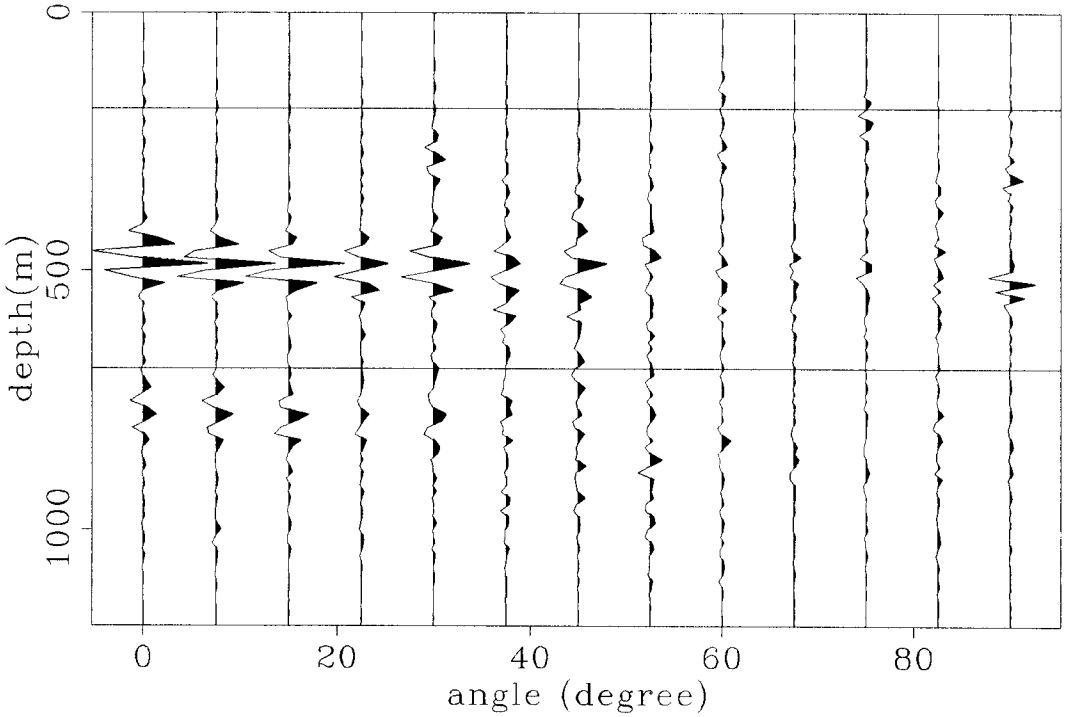

FIG. 4.14. Estimated plane-wave reflectivity function for the model of Figure 3.9.

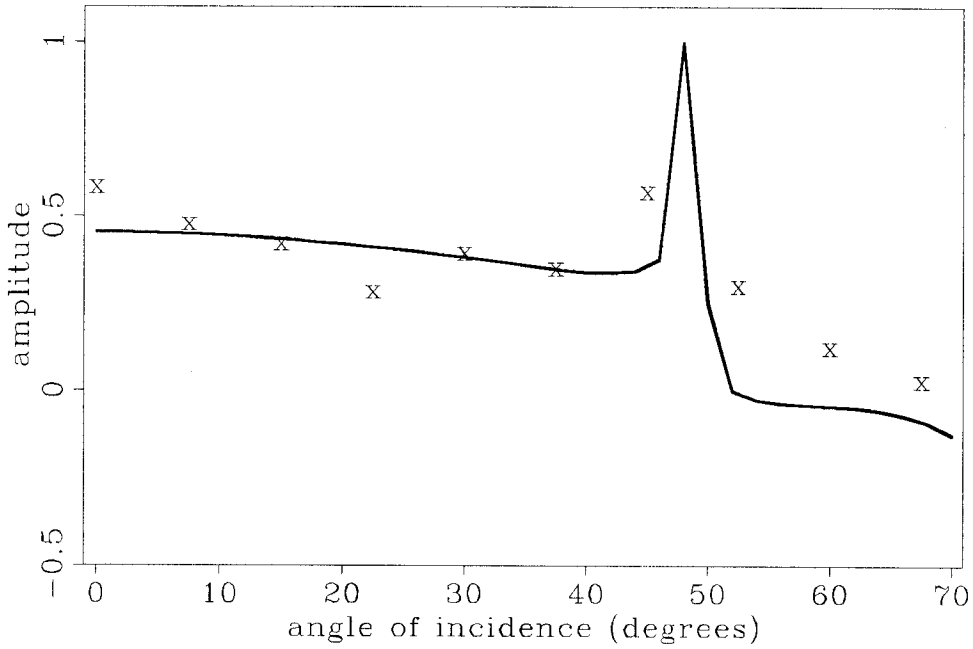

FIG. 4.15. Comparison between the analytical plane-wave response for the first interface of the model shown in Figure 3.9 (**continuous** line) and the plane-wave response estimated by the PWR migration (**X**'s).

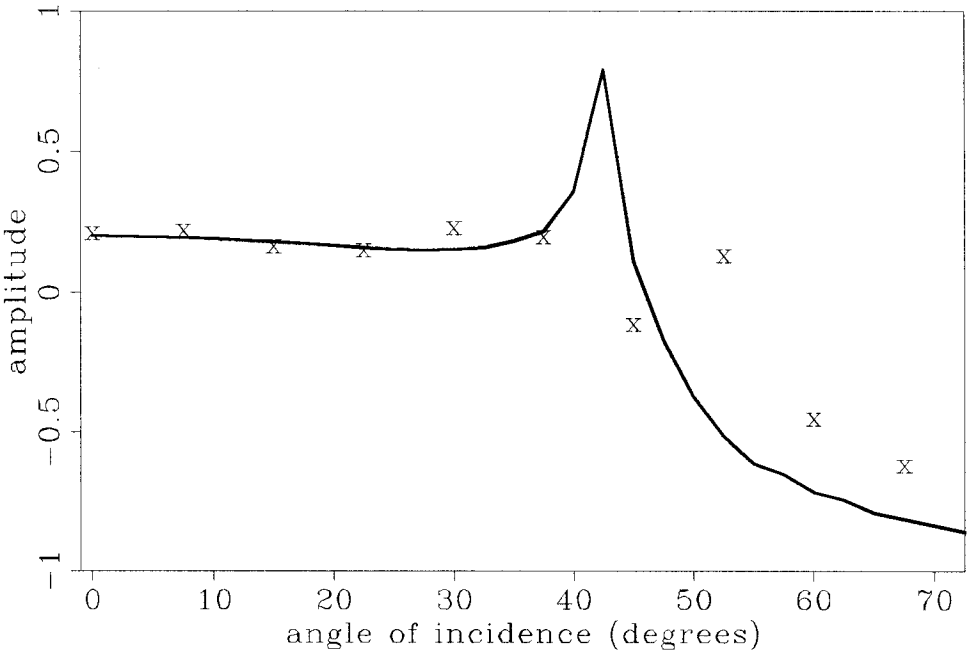

FIG. 4.16. Comparison between the analytical plane-wave response for the second interface of the model shown in Figure 3.9 (**continuous** line) and the plane-wave response estimated by the PWR migration (**X**'s).

also the accuracy of the discrete version of the integrals in equations 4.20 and 4.21. I believe that some of the misfit in Figures 4.15 and 4.16 are due to azimuthal aliasing associated with the poor angular coverage. However, I was not able to test this hypothesis because of the present core-memory restrictions.

One solution to overcome the limitations imposed by the core-memory availability is to reduce the angular aperture. This is not an easy task to execute not only because the rules derived in appendix B for the full 360 degrees angular aperture would have to be reviewed but also because the symmetry required for implementing the algorithm in a parallel architecture would be broken. Another solution involves the use of the static imaging condition instead of the [memory-bounded] dynamic imaging condition. However, to successfully apply the static imaging condition the upward-downward wavefield separation has to be based in a more elaborated method than the mask function technique in which the present implementation is based.

There are two theoretical limitations in the present formulation of the PWR migration. The first one is an intrinsic limitation of the plane-wave decomposition in heterogeneous media. Even though the wavefield is downward-continued to the local reflector point,

the radial integration to obtain the plane-wave response extends to the boundaries of the model. Only the part of the wavefield that lies inside the local Fresnel zone will contribute to the integral. As a result, the [theoretically] perfect estimation of the plane-wave reflectivity is restricted to the cases in which the minimum thickness of a layer is larger than the Fresnel zone of the waves inside that layer. The other theoretical limitation is not intrinsic but related to the finite size of the model (model aperture) and to the plain plane-wave decomposition method applied in the present implementation. At later times, when the primary wavefronts reach the boundaries of the model, the radial integration will not give the correct value for the plane-wave components not only because of the missing information beyond the boundary, but also because of the presence of the absorbing region near the boundary. Solutions to overcome this limitation involve either the use of a more sophisticated decomposition method that accounts for the finite aperture of the model, or the use of an oversized model which suffers the same core-memory restrictions discussed before.

4.5 Summary

In structurally complex media, the accurate recovery of the angle-dependent reflectivity function requires the use of an elastic prestack migration technique. Mode separation can be done before depth extrapolation or during the imaging step. Though more complex, the latter is more complete because it allows the imaging of mode-converted waves. The standard crosscorrelation criterion for implementing the imaging condition is not suitable for true reflectivity recovery, especially when imaging reflectivities that are associated with mode-converted waves. Two new alternative criteria were defined to overcome the limitations of correlation-based imaging conditions. The V-stack criterion accounts for conversion losses of the downgoing wavefield and avoids the imaging of false events associated with an unsmoothed background velocity model. The plane-wave-response criterion not only offers the same advantages, but also is designed to generate images that can be directly related to the Zoeppritz equations, since they represent the in-depth plane-wave response of the medium. This criterion is merged with a one-experiment, time-dependent-boundary-condition approach to wavefield extrapolation to define the plane-wave-response (PWR) migration. Results obtained with the application of the PWR migration to synthetic data validate the theoretical formulation.